Multiphoton Absorption and Graphitization in Poly(methyl methacrylate)-Coated Aluminium Nanoantenna Arrays

*Kamonpan Chumpol, Niall McEvoy, Xia Zhang‡, and Richard G. Hobbs**

Centre for Research on Adaptive Nanostructures and Nanodevices (CRANN), Advanced Materials and Bio-Engineering Research Centre (AMBER) and School of Chemistry, University of Dublin, Trinity College, College Green, Dublin 2, Ireland

‡School of Physics, University of Dublin, Trinity College, College Green, Dublin 2, Ireland

ABSTRACT: Collective electron oscillations, termed surface plasmons, in subwavelength metallic nanostructures can be excited by light, giving rise to an enhanced optical near-field at the surface of the metal. This field enhancement decays with distance away from the surface of the metal while the surface plasmon can decay due to energy transfer to the metal and surrounding materials. This energy transfer, previously considered detrimental for applications in photonics, shows promise for photocatalysis and energy conversion by exploiting the enhanced light-matter interactions present in plasmonic materials. However, insight into the chemical mechanism of energy transfer within the optical near-field is relatively elusive. Here we propose a method to investigate plasmon-driven chemical transformations in poly(methyl methacrylate) (PMMA) using aluminium nanostructures having surface plasmon modes that are resonant with laser illumination at λ = 532 nm. Surface-plasmon-driven chemical changes in PMMA were observed by Raman spectroscopy. Specifically, graphitic carbon was observed to form on plasmonic nanostructures. The volume of exposed PMMA was observed to scale with the second power of the laser intensity, which is consistent with a two-photon absorption process. This observation suggests that two-photon absorption drives polymer-chain scission, resulting in the transformation of PMMA into graphitic carbon.

INTRODUCTION

Sub-wavelength metallic nanostructures can act as antennas to efficiently convert electromagnetic radiation into other forms of energy (chemical, thermal) locally on the nanoscale.[1] The ability to confine light to nanoscale volumes is particularly interesting for high-resolution nanoimaging applications that require imaging at length scales beyond the diffraction limit,[2] but also benefits applications such as photochemistry, photocatalysis, and sensing.[3–15] These applications are made possible due to the excitation of localized surface plasmon resonances (LSPRs), collective oscillations of charge carriers in the nanostructured metal that are resonant with incident radiation.[16]

Nanostructure geometry (shape, size, particle-particle separation) and composition of the surrounding medium are key parameters for tuning LSPRs.[17] The metal composition also plays a vital role in defining the spectral range of LSPRs. Plasmon tunability ranges in commonly used noble metals such as Au, Cu, and Ag fall primarily in the visible and infrared regions of the spectrum,[18] which limits their use for applications that require light harvesting in the mid- or deep-UV regions. Although Au has been widely studied for biomedical applications due to its excellent resistance to corrosion and oxidation, associated costs are prohibitive to the scalability of technologies based on Au materials. Ag nanoparticles have a broad plasmon tuneability range from approximately 350 nm to the visible region and are promising candidates for electronic devices due to the high electrical and thermal conductivity of Ag. However, Ag tarnishes readily by reacting with sulfur to form surface sulfide films, which lead to degradation of plasmonic performance.[19,20]

In recent years, Al has received significant attention for plasmonic applications in the UV and visible regions of the spectrum. Aluminium is an interesting plasmonic material due to practical

advantages over noble metals like Au and Ag such as greater natural abundance and lower cost.[20,21] Additionally, under ambient conditions Al forms a self-limiting surface oxide layer with a thickness of approximately 3 nm. This oxide layer can serve as a protective film that prevents further oxidation.[22]

LSPRs can give rise to extreme confinement of electromagnetic radiation on the nanometer scale at the surface of metals. This electromagnetic near-field enhancement decays with distance away from the surface of the metal, while the enhanced fields can decay by transferring energy to phonons, hot carriers, and photons, which can be exploited in a variety of applications. For instance, photothermal therapy can potentially make use of heat generated by plasmonic materials to destroy cancer cells,[23] while photocatalysis and energy conversion applications avail of hot carriers generated during plasmon decay to drive chemical reactions.[10,24] In biosensing applications, plasmonic antennas can amplify or enhance fluorescence signals of fluorophores (e.g. organic dyes or quantum dots) for improved clinical analysis that can shorten diagnostic times.[25,26] In order to optimize the performance of these plasmon-assisted applications, it is essential to understand energy transfer to materials including energy transfer mechanisms in plasmonic nanoantennas at the single-antenna level.

Poly(methyl methacrylate) (PMMA) – commonly used as electron-beam lithography resist – has now been extended to study the near-field energy transfer from plasmonic antennas by groups of researchers including Volpe's[9] and Hobbs'.[8] In their work, high-intensity pulsed lasers were used to achieve near-field mapping of nanoantennas by observing morphological and chemical changes in electron-beam resists. Separately, continuous-wave (CW) laser with a wavelength of approximately 640 nm has been used to study plasmon-induced polymerization on Au and Ag nanoparticles.[4,7] The polymer was found to form around metallic nanoparticles where the strong

field enhancement occurred. It is suggested that the near-field distribution of energy transfer can simply be mapped using a CW laser excitation source.

Here, we propose a simple method to investigate the near-field distribution of energy transfer from Al nanoantennas using plasmon-enhanced chemical transformations in PMMA excited with a CW laser. Electron energy-loss spectroscopy and cathodoluminescence have been used previously to probe the near field of plasmonic Al nanoantennas.[27,28] However, at the time of writing we are unaware of the use of chemical transformations in polymer thin films to probe near-field energy transfer for Al nanoantennas. In this work, we use plasmon-enhanced decomposition of PMMA in the near-field of Al bowtie and nanodisk antennas to investigate near-field energy transfer.

The use of a CW diode laser (λ = 532 nm) is advantageous in terms of the simplicity of the apparatus, as well as the lower cost. The distribution of energy transfer into PMMA was observed through the volume of decomposed PMMA surrounding Al nanoantennas. Interestingly, PMMA was reported to convert into sp^2 hybridized carbon[29,30] when exposed to electron beam[31] or energetic ions.[32] In our work, through the contribution of Al plasmonic materials, we also observed the transformation of PMMA into graphitic carbon using Raman spectroscopy.

EXPERIMENTAL SECTION

Numerical Method. Finite-difference time-domain (FDTD) simulations with a commercial software package (*Lumerical Solutions Inc*., version: 8.20.1661) were used to calculate the optical field enhancement of Al nanoantennas and to design Al nanoantennas having LSPRs at 532 nm matching the laser excitation wavelength in the Raman spectroscopy system. Optical scattering and absorption of Al bowtie and nanodisk antennas were simulated. Al bowties consisted of two

tip-to-tip equilateral triangles with an edge-length of 85 nm, a thickness of 20 nm and a gap of 15 nm. For more accurate results, we also modified the curvature of the corners of the bowtie (see figure 1). The radius of each corner was set to 10 nm to approximately match the fabricated antennas (see figure 2). Al nanodisks had a 100-nm diameter and a thickness of 20 nm. A 3-nm-thick surface-oxide layer was included in all simulations. These structures were simulated individually in air while the bottom surfaces were placed on an indium-doped-tin-oxide (ITO)-coated glass substrate. The ITO layer had a thickness of 100 nm while a bulk glass substrate was employed. The refractive indices of ITO and glass were taken from König *et al.*.[33] The dielectric functions of aluminium and aluminium oxide were taken from Palik.[34] Total-field scattered-field (TFSF) source with a spectral range of 350-700 nm was launched from the air above an isolated nanoantenna at normal incidence following the experimental configuration, with polarization along the *x*- and *y*-directions (see figure 1). A mesh unit of 2.5 × 2.5 × 2.5 nm^3 was used in all simulations. Perfectly matched layer (PML) was set as a boundary condition for all sides around the antenna to obtain the absorption and scattering cross-sections for a single antenna. To demonstrate that Al nanoantennas employed in this work provided the LSPRs that matched well with the excitation wavelength in the Raman spectroscopy, we additionally provide simulation results of Al nanoantennas with various dimensions (see figure S1 and S2).

Sample Preparation. Aluminium nanoantennas were fabricated on a transparent conductive substrate using electron beam lithography (EBL). The substrate purchased from *Ossila* consists of a 100-nm thick ITO layer coated on a soda-lime glass substrate. Prior to EBL writing, an ITO coated glass substrate (1.1 mm × 20 mm × 15 mm) was first cleaned using a 1% *Hellmanex* surfactant diluted in deionized water for 5 min in an ultrasonicator and rinsed by deionized water and isopropyl alcohol (IPA), respectively. The substrate was then treated by oxygen plasma –

Diener PICO barrel asher - with an oxygen pressure of 0.3 mbar and 100W power level for 3 min. A 70-nm-thick layer of PMMA (2% 950k PMMA in anisole, purchased from *MicroChem Corp*.) was spin-coated on the substrate at 3 krpm (acceleration rate of 2 krpm/s) for 1 min and the sample was baked at 180℃ for 2 min on a hotplate. The thickness of PMMA films was measured using ellipsometry. Film thicknesses were determined from spin curves measured on Si substrates. During EBL, the resist was patterned (*Zeiss SUPRA 40* with a *Raith Quantum* pattern generator) using a 7 μm objective aperture, an acceleration voltage of 15 kV and an areal dose of 1300 $\mu C/cm^2$. The measured electron-beam current was typically 18 pA. To achieve high-resolution patterning, a short working distance of approximately 3.5 mm was used. After exposure, the sample was developed using a 3:1 methyl-iso-butyl-ketone:isopropyl alcohol solution at a low temperature of 0℃ for 30 s. The cooling method was carried out using a thermoelectric cold plate with a stirring bar to promote a homogeneous temperature. The sample was then dried using a nitrogen spray gun. Following the development, a 20-nm-thick layer of aluminium was then deposited on the specimen by electron-beam evaporation using a *Temescal FC-2000* deposition system (1 Å/s deposition rate and 3.0×10^{-6} Torr base pressure), with the thickness measured by a quartz crystal monitor. The pattern was thereafter transferred to the substrate via a lift-off process by immersing the specimen in n-methylpyrrolidone (NMP) at 55℃ for 45 min. The sample was then rinsed in acetone and IPA, respectively prior to drying with a nitrogen spray gun.

Electron Microscopy. Al nanoantennas were inspected using a scanning electron microscope (*Zeiss ULTRA Plus*) before and after laser exposure. An electron beam with an acceleration voltage of typically 5 keV or 10 keV passing through a 30 μm aperture and a working distance of approximately 4.0 mm was used with an in-lens detection system.

UV-Vis Spectroscopy. Spectral measurements were carried out using an in-house setup. The system consisted of an inverted microscope (*Zeiss Axiovert 100M*) and a spectrometer (*Andor Kymera 328i*) integrated with an electron-multiplying CCD camera (*Newton 970, Andor*). A 40× objective (0.65 NA) collected light transmitted through the sample. The generated image was aligned to pass through the slit of the spectrometer. The setup configuration can be found in figure S3. A transmitted spectrum was then collected using integrated software (*Andor SOLIS*) with a 500-nm blazed grating at 150 l/mm. To acquire extinction spectra, Beer-Lambert law was applied.

Raman Spectroscopy. Laser exposure was carried out using a green laser (532 nm) in two different Raman microscope systems. To study the plasmon-assisted chemical changes in PMMA, we used a 532-nm CW laser in a Raman microscope (*WITec alpha300 R*), the beam was focused on the sample using a 100× (0.95 NA) objective to produce a spot with a nominal diameter of 300 nm and a laser power of 4.75 mW. A 5μm × 5μm Raman map was produced with an exposure time per step of 1 s, and step size of 500 nm. For the study of multiphoton absorption, we used a *Horiba* Raman spectroscopy system with a 100× (0.90 NA) objective and a varying laser power, while the remaining parameters were set similar to those in the aforementioned system.

RESULTS AND DISCUSSION

Optical Analysis. In this work, we used a CW laser with a wavelength of 532 nm to excite Al nanoantennas. FDTD simulations were used to design plasmonic nanoantennas having an LSPR near 532 nm and to calculate the electric field enhancement of nanoantennas when excited by linearly polarized 532-nm light, which is incident normal to the substrate surface. Figures 1a-b show simulation results indicating the polarization-dependent electric field enhancement for Al bowtie nanoantennas having a dipole resonance along the x-axis close to λ = 532 nm. Figure 1a

shows the electric field distribution around an Al bowtie nanoantenna for polarization along the *x*-axis. The electric field is enhanced with a maximum field intensity $|E|^2 \approx 102$, in the gap of the bowtie. When the incident light is polarized along the *y*-axis, as in figure 1b, an enhancement of the field intensity of nearly 20 times at the outer corners of the bowtie was observed. Figures 1c-d show the extinction (blue curve), absorption (grey curve) and scattering (red curve) spectra of an individual Al bowtie nanoantenna with the dimensions shown in figures 1a-b. The absorption and scattering cross-sections were calculated by FDTD simulation using incident light in the wavelength range from 350 nm to 700 nm. It is evident that when the nanoantenna was excited by *x*-polarized light the peak in the extinction spectrum was close to 532 nm, whereas when excited by *y*-polarized light, the absorption, scattering and extinction peaks were at a shorter wavelength. Extinction, absorption and scattering spectra were also calculated for bowtie nanoantennas having side lengths of 65 nm and 105 nm for comparison to those shown in figures 1c-d. These spectra are included in figure S1 and show that the antennas with a side length of 85 nm produce a dipole resonance whose wavelength most closely matches that of the laser used here.

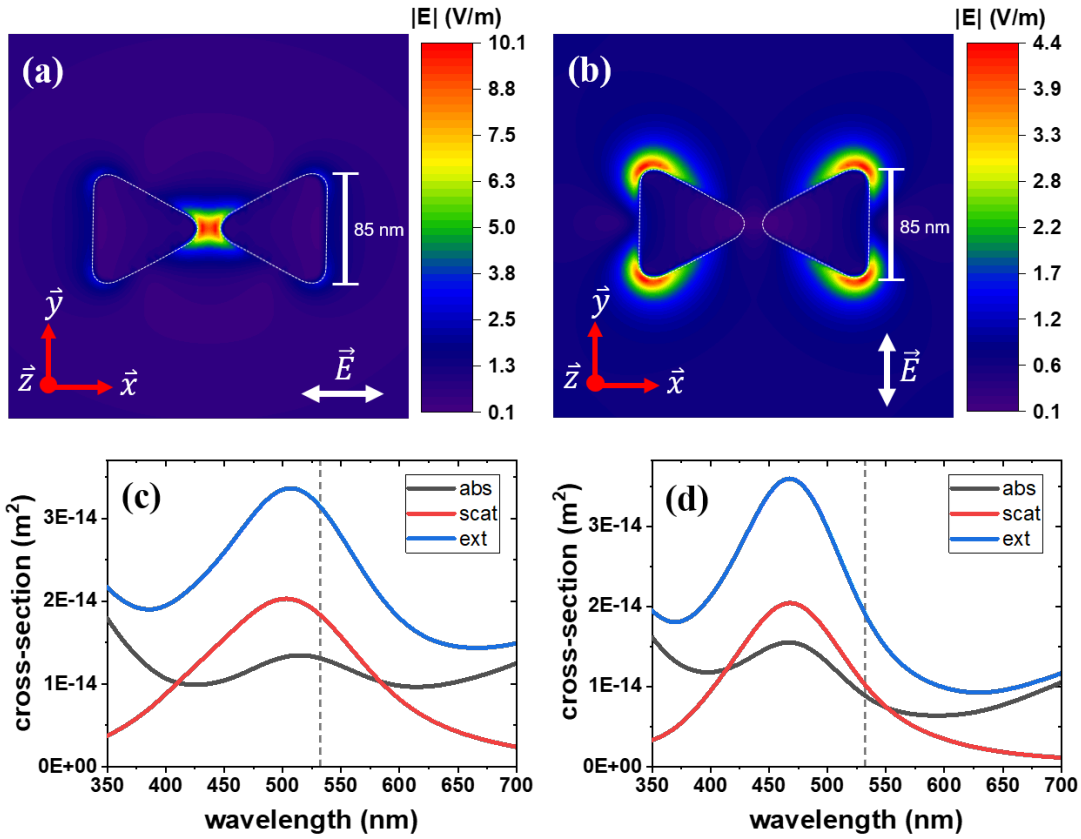

Figure 1. (a, b) Electric field distribution maps of an isolated bowtie nanoantenna calculated using FDTD method with *x*- and *y*-polarizations. The direction of polarization of incident light is indicated by $\vec{E}$, whereas the colour bars indicate the levels of field enhancement normal to the sample surface. **(c, d)** absorption (grey curve), scattering (red curve) and extinction (blue curve) spectra of the related antenna with *x*- and *y*-polarizations, respectively. The vertical dashed lines at 532 nm indicate the wavelength of the laser used in this experiment.

The field enhancement shown in figures 1a and 1b was calculated for an Al bowtie antenna consisting of two equilateral triangles with an edge length of 85 nm and a central gap of 15 nm. As a first test structure to demonstrate the potential of our approach, we fabricated our nanostructures with shapes and dimensions obtained from FDTD simulations using EBL on an ITO-coated glass substrate. The sample consisted of Al bowtie nanoantenna arrays having a

constant separation while the central gap was set to either 10 or 15 nm. The fabricated nanostructures had a period of 308 and 313 nm in the *x*-direction corresponding to central gaps of 10 nm and 15 nm, respectively, while the period in the *y*-direction for both arrays was 235 nm (see figure S4). SEM images in figure 2 show examples of Al bowtie nanoantennas fabricated using EBL. In this case, Al bowtie nanoantennas had a physical edge length of 85 ± 1 nm and a central gap of 15 ± 1 nm. Samples having a central gap of 15 nm are defined as g15 in this paper and samples with a central gap of 10 nm are defined as g10.

Al is considered an active metal *i.e.* it reacts rapidly with oxygen in air to form a surface layer of aluminium oxide (Al_2O_3). This surface layer grows spontaneously to a thickness of approximately 3 nm and thereafter acts as a protective layer to prevent further reaction.[10] As a consequence, the physical dimensions of the nanoantennas measured after nanofabrication have already included the thickness of aluminium oxide layer.

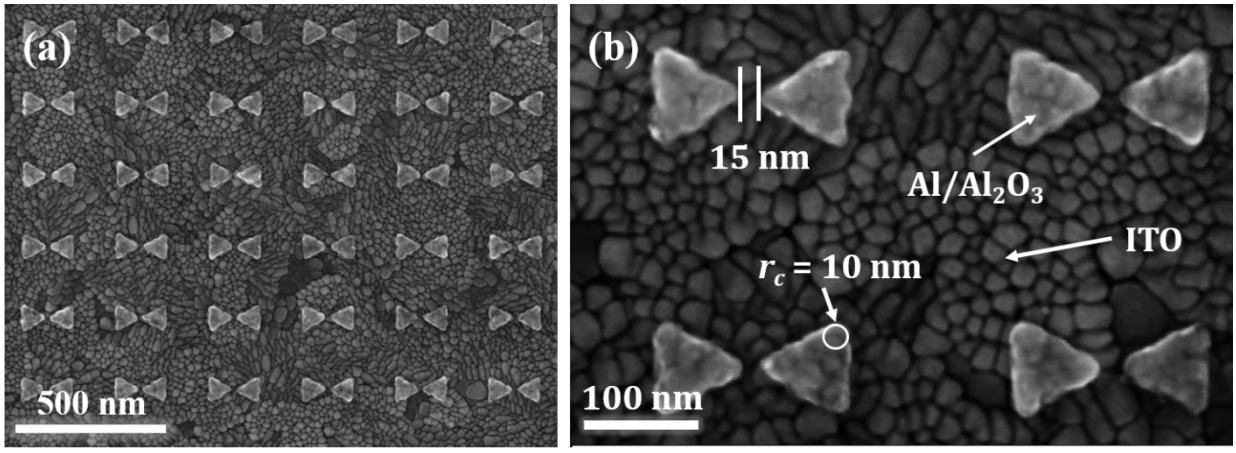

Figure 2. Scanning electron micrographs at low (**a**) and high (**b**) magnifications of Al bowtie nanoantenna array prepared on an ITO-coated glass substrate. The fabricated bowtie antennas have physical gaps measuring 15 ± 1 nm and corner radii of 10 ± 1 nm.

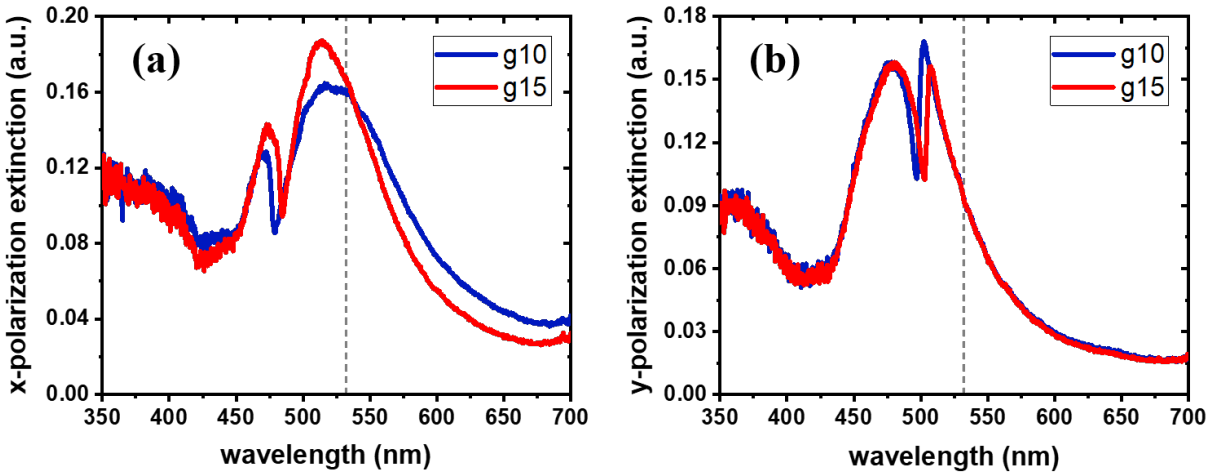

Figure 3. (**a, b**) Experimental extinction spectra of Al bowtie nanoantenna arrays with (**a**) *x*- and (**b**) *y*-polarizations. The data were collected from the bowties with a gap of 10 nm (g10 in blue) and 15 nm (g15 in red). The grey dashed lines indicate the 532-nm laser wavelength.

Figures 3a and 3b, show the experimentally measured extinction spectra of the sample with *x*- and *y*-polarizations, respectively. It should be noted that the experimental extinction spectra were collected from Al bowtie nanoantenna arrays and not from single nanoantennas, hence giving spectra that are distinct from those calculated using the FDTD simulations for an isolated antenna. The intriguing peak splitting displayed in figure 3 is likely due to coupling between the LSPRs and surface lattice resonances (SLRs), which may occur when the incident light is diffracted and scattered by periodic arrays of metallic nanostructures.[35] In figure 3a, although the peak splitting occurred for bowties with gaps of 10 and 15 nm the LSPRs still remain close to the laser wavelength of 532 nm, especially for the case of *x*-polarized light. Previous literature reports suggest that coupling between LSPRs and SLRs will not significantly modify the spatial distribution of the near field.[36]

Decomposition and Graphitization of PMMA in the Near-Field. A 42-nm-thick PMMA film was spin-coated on the nanoantenna arrays to act as a photosensitive molecular probe to study energy transfer in the near-field of the bowtie nanoantennas. Illumination was provided by a 532-nm CW laser in a Raman microscope (*WITec alpha300 R*) as described in the experimental section above. In the first test, a minimum incident power of 4.75 mW was used per exposure for 1 s. The sample was then immersed in a developer solution (MIBK:IPA 1:3 v/v) for 40 s at room temperature to remove the exposed areas of PMMA revealing regions where PMMA decomposed in the near-field of the bowtie nanoantennas. Figures 4a and 4b show SEM micrographs of the areas of decomposed PMMA around a bowtie after development. SEM micrographs showing the clear contrast between exposed and unexposed nanoantennas can be found in figure S5.

Moreover, we have investigated the effect of laser polarization on PMMA decomposition in the near-field of Al nanoantennas. Figure S6 shows SEM images of bowtie nanoantennas after laser exposure and removal of decomposed PMMA. The study suggests that polarization along the *x*-axis leads to greater PMMA decomposition, which correlates well with the simulation results provided in figure 1 and supports an exposure mechanism involving LSPRs in the nanoantennas.

In addition to imaging PMMA decomposition in the near-field of the nanoantennas by electron microscopy, we also observed chemical changes in PMMA through Raman fingerprints. Figures 4c and 4d show the Raman spectra of PMMA-coated Al bowtie nanoantenna arrays with gaps of 10 nm and 15 nm, respectively. The two peaks at approximately 1350 cm^{-1} and 1587 cm^{-1} correlate well with D- and G-bands expected for graphitic carbon and represent sp^2 hybridized carbon[20-22]. In order to investigate whether Al nanoantennas play an important role in contributing to the chemical changes in PMMA, we also collected Raman spectra of pure PMMA from regions on the substrate where Al nanoantennas were not present. Figure 4e shows an average result of

Raman spectra obtained from pure PMMA films. The Raman peak at 1087 cm^{-1} is intrinsic to PMMA[37] and appeared on both spectra where Al bowties were and were not present. Similar results were observed for both PMMA-coated Al bowtie nanoantennas with gaps of 10 nm and 15 nm suggesting that PMMA conversion into graphitic material is driven by surface plasmons in Al nanostructures.

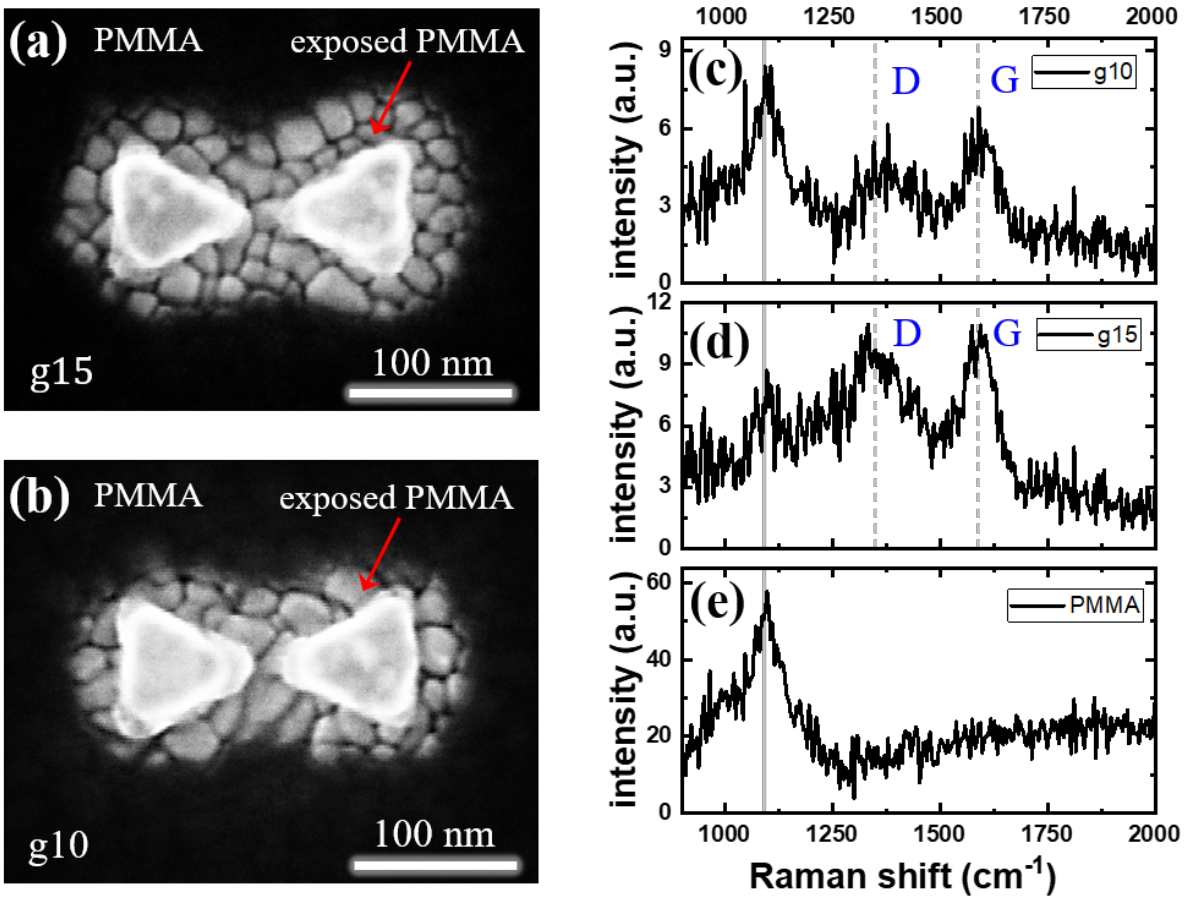

Figure 4. (**a, b**) Decomposed PMMA around Al bowtie antennas in the near-field. (**c, d**) Raman spectra of PMMA-coated Al nanoantenna arrays with central gaps of 10 nm and 15 nm, respectively and (**e**) Raman spectrum of pure PMMA films. The grey solid line at 1087 cm^{-1} is characteristic of PMMA, while the grey dashed lines at 1350 cm^{-1} and 1587 cm^{-1} correspond to D- and G- bands present in graphitic carbon.

Multiphoton Absorption Analysis. Many works have been reported in the literature that investigate the mechanisms by which plasmonic nanoantennas enhance photocatalytic processes. The roles of hot electrons and holes, localized heating as well as surface electric fields have been investigated regularly.[3,6,38] Volpe *et al.*[9] previously reported that PMMA exposure on Au nanoantennas excited by a near-infrared femtosecond laser could be explained by a multiphoton absorption mechanism by measuring the volume of exposed PMMA in the near-field of nanorod antennas as a function of laser intensity. Here, we take a similar approach to investigate PMMA exposure on Al nanodisk antennas excited by a CW laser. We fabricated a sample consisting of Al nanodisk arrays on an ITO-coated substrate. Al nanodisks had diameters of 100 nm and were separated by 350 nm in a square array (see figure S4). An experimental extinction spectrum of Al nanodisk array correlating with the excitation wavelength is shown in figure S8 in the Supporting Information. The sample was inspected using an SEM as shown in figure 5a. The symmetry of the nanodisks simplifies calculation of the decomposed volume of PMMA in the near-field of the nanodisks after laser exposure (see figure S7). Calculations of the volume of decomposed PMMA are presented in the Supporting Information (tables S1-S3). The standard deviation of at least 10 measurements for each volume is provided.

In figure 5c, the volume of decomposed PMMA was observed to vary with the laser power in the power range from 9.6 to 17.1 mW. Additional SEM images showing decomposed PMMA around Al nanodisks can be found in figure S9. The volume of decomposed PMMA surrounding Al nanodisks increased with increasing laser power as shown in figure 5b. The volume of exposed PMMA was observed to scale with laser power according to a second-order power function (red dashed curve figure 5b).

To further analyze our experimental data, we used the Beer-Lambert law as a model to better understand the exposure mechanism in PMMA. From the Beer-Lambert law, $\frac{\mathrm{d}I}{\mathrm{d}x} = -\propto_n I^n$, the decay in the intensity of light, I, at a depth, x, in a material is proportional to a coefficient, $\propto_n$ where n is the number of photons absorbed. In the case of our experiment, we have studied the volume of exposed PMMA, V, as a function of the laser power, P, which is directly proportional to the laser intensity at the sample. From the Beer-Lambert law, we can then relate the exposed volume to the laser power by, $V \propto P^n$. A second-order power function was found to best fit the data in the graph in figure 5b, which suggested that a two-photon absorption process was involved in the polymer-chain scission leading to chemical transformations of PMMA into graphitic materials.

PMMA is reported to have an optical band gap in the 4-5 eV range.[39–42] A photon with a free-space wavelength of 532 nm carries 2.33 eV and consequently, two such photons may possess sufficient energy to excite PMMA via this optical band gap. We tentatively suggest that the exposure of PMMA observed in this work is related to 2-photon absorption across this optical band gap, although further work is required to develop a mechanism for the observed PMMA exposure.

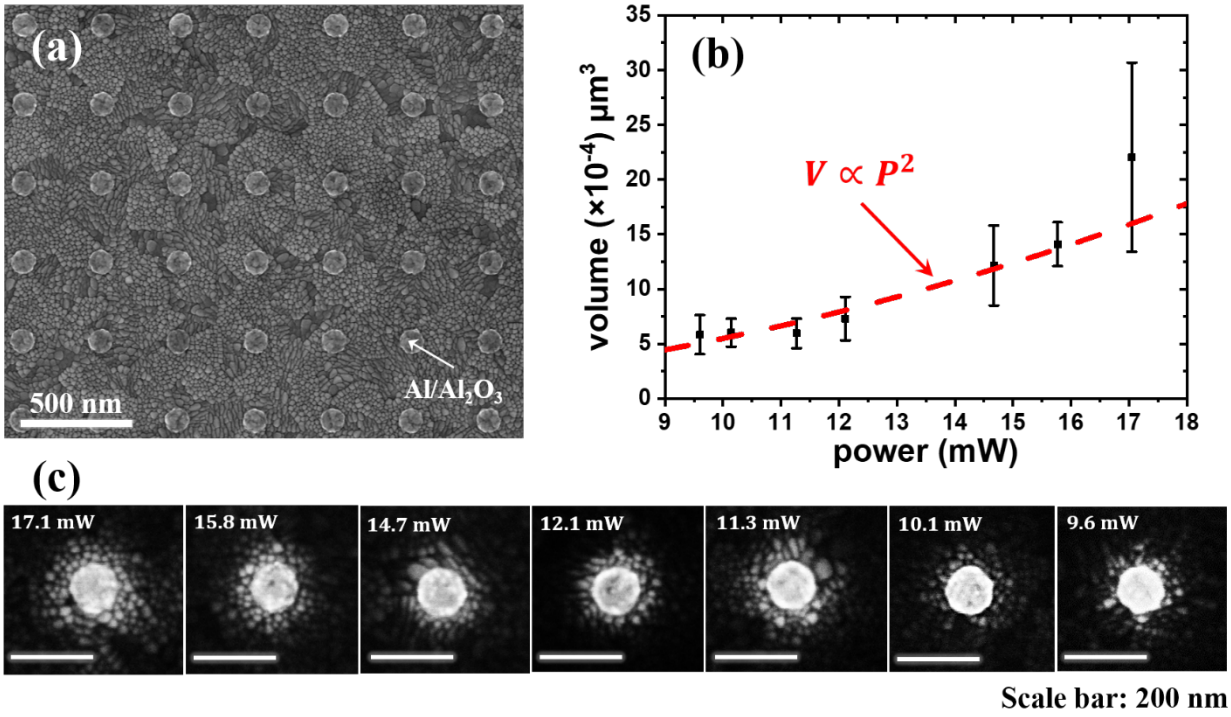

Figure 5. (**a**) Scanning electron micrograph of Al nanodisk array. (**b**) and (**c**) Power dependence of the decomposed PMMA volume around Al nanodisks. (**b**) The black squares in the graph represent the decomposed volume (V) of PMMA (with corresponding standard deviations in vertical black lines) as a function of incident laser power (P). The red dashed line in the graph represents the best fit to the data of a second-order power function (R-squared value of 0.92), which indicates a two-photon absorption mechanism. (**c**) SEM images of the respective decomposed volume of PMMA around Al nanodisks as a function of incident power. The minimum incident laser power used to achieve the polymer chain scission in PMMA for this particular structure was 9.6 mW.

Electron-Beam Irradiation and Graphitization in PMMA. Studies have shown that electron-beam exposure of PMMA causes graphitization of the polymer at high electron-beam energy (200 kV)[22] or low energy (10 kV) with post-exposure thermal annealing (800°C).[43] PMMA cross-

links under these exposure conditions and such cross-linking may be initiated by knock-on damage *i.e*. hydrogen and oxygen atoms displaced by energetic electrons and expelled as gases, leaving carbon atoms that can reassemble to form sp^2 hybridized networks.

To gain insight into how electron-beam irradiation affects the graphitization of PMMA with the existence of Al nanoantennas, we used electron-beam lithography to study electron-beam irradiation of PMMA-coated Al bowtie and nanodisk antennas with a relatively low operating voltage of 15 kV. By opting for a beam spot exposure instead of the usual raster scan, we can selectively expose small regions of interest. For the bowties, we allowed the central gaps to be exposed to the electron beam, while for the nanodisks, the exposure was performed at the edges of the nanodisks. These areas of interest correspond to the regions of maximum field enhancement when excited by the 532-nm laser. To be consistent, each electron beam exposure was for 15 s. This electron-beam irradiation was carried out prior to immersion of the sample into a chemical developer. The sample was then characterized by Raman spectroscopy.

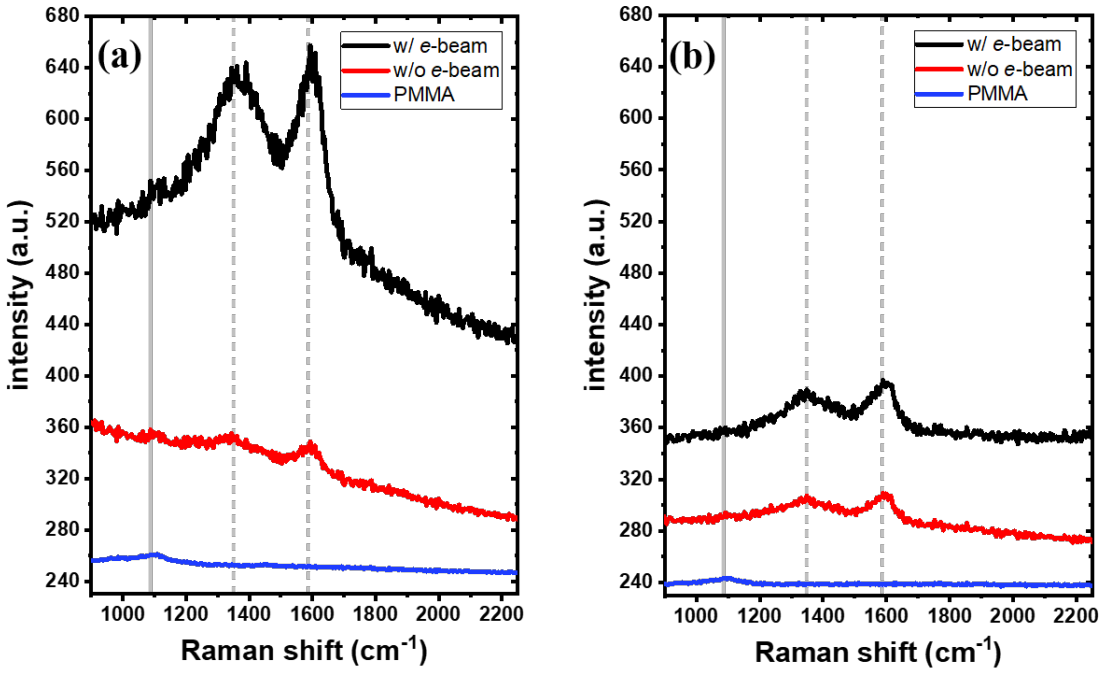

Figure 6. Raman spectra of PMMA coated on (**a**) Al bowtie nanoantenna arrays and (**b**) Al nanodisk arrays with (black curves) and without (red curves) the treatment of electron-beam irradiation prior to the Raman experiment. The blue curves represent the Raman spectra of isolated PMMA deposited on the same substrate. The vertical grey solid lines at 1087 cm^{-1} indicate a characteristic of PMMA while the vertical grey dashed lines at 1350 cm^{-1} and 1587 cm^{-1} are correlated to the D- and G-bands, respectively.

Raman spectra of PMMA-coated Al bowties and Al nanodisks are displayed in figures 6a and 6b, respectively. It is evident that with the treatment of electron-beam irradiation prior to Raman characterization, the Raman signals (black curves) of PMMA on both bowties and nanodisks are greater than those (red curves) without electron-beam treatment. However, the increasing relative intensity of the spectra from samples treated by the electron beam is different for the bowties and nanodisks. That is, for the bowties there is a greater enhancement of the Raman signal than for the

nanodisks, suggesting that shape, size, and geometry of metallic nanoantennas can potentially determine the degree of graphitization as well as providing single-particle-level analysis by Raman spectroscopy. The spectra in figure 6 show that plasmonic Al nanoantennas can generate local graphitization of PMMA in plasmonic hotspots as was shown earlier in figure 4 and can also enhance Raman signals from carbon nanodots graphitized by electron-beam exposure.

CONCLUSIONS

In conclusion, we have proposed and tested a method to map the near-field distribution of Al nanoantennas using a CW laser in a Raman spectroscopic system. The same method also allowed us to observe plasmon-driven chemical transformations in PMMA. Aluminium – a cheap, abundant and air-stable material – is shown to be a viable alternative to noble-metal plasmonic materials that can serve applications not only in the UV range, but also in the visible region (*i.e.* at 532 nm).

Tunable localized surface plasmon resonances in Al nanostructures are capable of generating a strong optical near-field at the nanostructure surface when excited by resonant incident illumination. The strong optical enhancement can drive multiphoton absorption in a material surrounding the metal *i.e.* PMMA. We have shown that the absorbed energy was consistent with a two-photon absorption mechanism and resulted in local graphitization of PMMA. The graphitization can not only be generated by a CW laser, but also by electron-beam irradiation. The evidence in Raman spectra reveals that the synergy between electron-beam irradiation and Al plasmonic nanoantennas could contribute to more complete graphitization of the polymer, even using low-energy electron-beam irradiation and may provide a route to generate plasmon-enhanced carbon nanodot structures for applications as sensors and photocatalysts.

ASSOCIATED CONTENT

Supporting Information. The Supporting Information is available free of charge on the ACS Publications website: experimental and calculated optical responses of Al nanoantennas, a polarization-dependent study on the decomposed PMMA volume, design and geometry of Al nanoantennas, calculation analysis of the decomposed PMMA volume based on symmetrical shape of Al nanodisks, and illustration of the optical setup for optical measurements.

AUTHOR INFORMATION

Corresponding Author

*E-mail: hobbsr@tcd.ie.

ACKNOWLEDGEMENT

The authors acknowledge the support of Dr. Eoin McCarthy, Dermot Daly, and Dr. Clodagh Dooley from the Advanced Microscopy Laboratory (AML); Dr. Julia Kremer and Neal O'Hara from the Centre for Research on Adaptive Nanostructures and Nanodevices (CRANN); and Dr. Calin Hrelescu from School of Physics, University of Dublin, Trinity College for training and technical support. RGH acknowledges financial support from the Royal Society-Science Foundation Ireland University Research Fellowship.

REFERENCES

(1) Novotny, L.; Van Hulst, N. Antennas for Light. *Nat. Photonics* **2011**, *5*, 83–90.
(2) Kawata, S.; Inouye, Y.; Verma, P. Plasmonics for Near-Field Nano-Imaging and Superlensing. *Nat. Photonics* **2009**, *3*, 388–394.
(3) Seemala, B.; Therrien, A. J.; Lou, M.; Li, K.; Finzel, J. P.; Qi, J.; Nordlander, P.; Christopher, P. Plasmon-Mediated Catalytic O2 Dissociation on Ag Nanostructures: Hot Electrons or Near Fields? *ACS Energy Lett.* **2019**, *4*, 1803–1809.
(4) Ding, T.; Mertens, J.; Lombardi, A.; Scherman, O. A.; Baumberg, J. J. Light-Directed Tuning of Plasmon Resonances via Plasmon-Induced Polymerization Using Hot Electrons.

ACS Photonics **2017**, *4*, 1453–1458.
(5) Robatjazi, H.; Zhao, H.; Swearer, D. F.; Hogan, N. J.; Zhou, L.; Alabastri, A.; McClain, M. J.; Nordlander, P.; Halas, N. J. Plasmon-Induced Selective Carbon Dioxide Conversion on Earth-Abundant Aluminum-Cuprous Oxide Antenna-Reactor Nanoparticles. *Nat. Commun.* **2017**, *8*, 1–9.
(6) Cortés, E.; Xie, W.; Cambiasso, J.; Jermyn, A. S.; Sundararaman, R.; Narang, P.; Schlücker, S.; Maier, S. A. Plasmonic Hot Electron Transport Drives Nano-Localized Chemistry. *Nat. Commun.* **2017**, *8,* 1–10.
(7) Wang, Y.; Wang, S.; Zhang, S.; Scherman, O. A.; Baumberg, J. J.; Ding, T.; Xu, H. Plasmon-Directed Polymerization: Regulating Polymer Growth with Light. *Nano Res.* **2018**, *11*, 6384–6390.
(8) Hobbs, R. G.; Putnam, W. P.; Fallahi, A.; Yang, Y.; Kärtner, F. X.; Berggren, K. K. Mapping Photoemission and Hot-Electron Emission from Plasmonic Nanoantennas. *Nano Lett.* **2017**, *17*, 6069–6076.
(9) Volpe, G.; Noack, M.; Aćimović, S. S.; Reinhardt, C.; Quidant, R. Near-Field Mapping of Plasmonic Antennas by Multiphoton Absorption in Poly(Methyl Methacrylate). *Nano Lett.* **2012**, *12*, 4864–4868.
(10) Ma, X. C.; Dai, Y.; Yu, L.; Huang, B. B. Energy Transfer in Plasmonic Photocatalytic Composites. *Light Sci. Appl.* **2016**, *5,* 1–13.
(11) Swearer, D. F.; Leary, R. K.; Newell, R.; Yazdi, S.; Robatjazi, H.; Zhang, Y.; Renard, D.; Nordlander, P.; Midgley, P. A.; Halas, N. J.; Ringe, E. Transition-Metal Decorated Aluminum Nanocrystals. *ACS Nano* **2017**, *11*, 10281–10288.
(12) Zhou, L.; Tan, Y.; Wang, J.; Xu, W.; Yuan, Y.; Cai, W.; Zhu, S.; Zhu, J. 3D Self-Assembly of Aluminium Nanoparticles for Plasmon-Enhanced Solar Desalination. *Nat. Photonics* **2016**, *10*, 393–398.
(13) Swearer, D. F.; Robatjazi, H.; Martirez, J. M. P.; Zhang, M.; Zhou, L.; Carter, E. A.; Nordlander, P.; Halas, N. J. Plasmonic Photocatalysis of Nitrous Oxide into N2 and O2 Using Aluminum-Iridium Antenna-Reactor Nanoparticles. *ACS Nano* **2019**, *13*, 8076–8086.
(14) Thangamuthu, M.; Santschi, C.; Martin, O. J. F. Photocatalytic Ammonia Production Enhanced by a Plasmonic Near-Field and Hot Electrons Originating from Aluminium Nanostructures. *Faraday Discuss.* **2019**, *214* , 399–415.
(15) Swearer, D. F.; Zhao, H.; Zhou, L.; Zhang, C.; Robatjazi, H.; Martirez, J. M. P.; Krauter, C. M.; Yazdi, S.; McClain, M. J.; Ringe, E.; Carter, E. A.; Nordlander, P.; Halas, N. J. Heterometallic Antenna-Reactor Complexes for Photocatalysis. *Proc. Natl. Acad. Sci. U. S. A.* **2016**, *113*, 8916–8920.
(16) Zeng, P.; Cadusch, J.; Chakraborty, D.; Smith, T. A.; Roberts, A.; Sader, J. E.; Davis, T. J.; Gómez, D. E. Photoinduced Electron Transfer in the Strong Coupling Regime: Waveguide–Plasmon Polaritons. *Nano Lett.* **2016**, *16*, 2651–2656.
(17) Li, X. D.; Chen, T. P.; Liu, Y.; Leong, K. C. Influence of Localized Surface Plasmon Resonance and Free Electrons on the Optical Properties of Ultrathin Au Films: A Study of the Aggregation Effect. *Opt. Express* **2014**, *22*, 5124–5132.
(18) Lal, S.; Link, S.; Halas, N. J. Nano-Optics from Sensing to Waveguiding. *Nat. Photonics* **2007**, *1*, 641–648.
(19) Rycenga, M.; Cobley, C. M.; Zeng, J.; Li, W.; Moran, C. H.; Zhang, Q.; Qin, D.; Xia, Y. Controlling the Synthesis and Assembly of Silver Nanostructures for Plasmonic

Applications. *Chem. Rev.* **2011**, *111*, 3669–3712.
(20) Knight, M. W.; King, N. S.; Liu, L.; Everitt, H. O.; Nordlander, P.; Halas, N. J. Aluminum for Plasmonics. *ACS Nano* **2014**, *8*, 834–840.
(21) Gutiérrez, Y.; de la Osa, R. A.; Ortiz, D.; Saiz, J. M.; González, F.; Moreno, F. Plasmonics in the Ultraviolet with Aluminum, Gallium, Magnesium and Rhodium. *Appl. Sci.* **2018**, *8,* 1–14.
(22) Langhammer, C.; Schwind, M.; Kasemo, B.; Zorić, I. Localized Surface Plasmon Resonances in Aluminum Nanodisks. *Nano Lett.* **2008**, *8*, 1461–1471.
(23) Huang, X.; El-Sayed, M. A. Plasmonic Photo-Thermal Therapy (PPTT). *Alexandria J. Med.* **2011**, *47*, 1–9.
(24) Brongersma, M. L.; Halas, N. J.; Nordlander, P. Plasmon-Induced Hot Carrier Science and Technology. *Nat. Nanotechnol.* **2015**, *10*, 25–34.
(25) Bauch, M.; Toma, K.; Toma, M.; Zhang, Q.; Dostalek, J. Plasmon-Enhanced Fluorescence Biosensors: A Review. *Plasmonics*. **2014**, *9*, 781–799.
(26) Lakowicz, J. R. Radiative Decay Engineering 5: Metal-Enhanced Fluorescence and Plasmon Emission. *Anal. Biochem.* **2005**, *337*, 171–194.
(27) Knight, M. W.; Liu, L.; Wang, Y.; Brown, L.; Mukherjee, S.; King, N. S.; Everitt, H. O.; Nordlander, P.; Halas, N. J. Aluminum Plasmonic Nanoantennas. *Nano Lett.* **2012**, *12*, 6000–6004.
(28) Hobbs, R. G.; Manfrinato, V. R.; Yang, Y.; Goodman, S. A.; Zhang, L.; Stach, E. A.; Berggren, K. K. High-Energy Surface and Volume Plasmons in Nanopatterned Sub-10 nm Aluminum Nanostructures. *Nano Lett.* **2016**, *16*, 4149–4157.
(29) Casiraghi, C.; Pisana, S.; Novoselov, K. S.; Geim, A. K.; Ferrari, A. C. Raman Fingerprint of Charged Impurities in Graphene. *Appl. Phys. Lett.* **2007**, *91,*1–3.
(30) Verzhbitskiy, I. A.; De Corato, M.; Ruini, A.; Molinari, E.; Narita, A.; Hu, Y.; Schwab, M. G.; Bruna, M.; Yoon, D.; Milana, S.; Feng, X.; Müllen, K.; Ferrari, A. C.; Casiraghi, C.; Prezzi, D. Raman Fingerprints of Atomically Precise Graphene Nanoribbons. *Nano Lett.* **2016**, *16*, 3442–3447.
(31) Duan, H.; Xie, E.; Han, L.; Xu, Z. Turning PMMA Nanofibers into Graphene Nanoribbons by In Situ Electron Beam Irradiation. *Adv. Mater.* **2008**, *20*, 3284–3288.
(32) Koval, Y. Mechanism of Etching and Surface Relief Development of PMMA under Low-Energy Ion Bombardment. *J. Vac. Sci. Technol. B* **2004**, *22*, 843–851.
(33) König, T. A. F.; Ledin, P. A.; Kerszulis, J.; Mahmoud, M. A.; El-Sayed, M. A.; Reynolds, J. R.; Tsukruk, V. V. Electrically Tunable Plasmonic Behavior of Nanocube-Polymer Nanomaterials Induced by a Redox-Active Electrochromic Polymer. *ACS Nano* **2014**, *8*, 6182–6192.
(34) Palik, E. D. *Handbook of Optical Constants of Solids*; Academic Press, 1998.
(35) Kravets, V. G.; Kabashin, A. V.; Barnes, W. L.; Grigorenko, A. N. Plasmonic Surface Lattice Resonances: A Review of Properties and Applications. *Chem. Rev.* **2018**, *27*, 5912–5951.
(36) Wang, W.; Ramezani, M.; Väkeväinen, A. I.; Törmä, P.; Rivas, J. G.; Odom, T. W. The Rich Photonic World of Plasmonic Nanoparticle Arrays. *Mater. Today* **2018**, *21*, 303–314.
(37) Thomas, K. J.; Sheeba, M.; Nampoori, V. P. N.; Vallabhan, C. P. G.; Radhakrishnan, P. Raman Spectra of Polymethyl Methacrylate Optical Fibres Excited by a 532 Nm Diode Pumped Solid State Laser. *J. Opt. A Pure Appl. Opt.* **2008**, *10*, 1–6.
(38) Yu, Y.; Sundaresan, V.; Willets, K. A. Hot Carriers versus Thermal Effects: Resolving the

Enhancement Mechanisms for Plasmon-Mediated Photoelectrochemical Reactions. *J. Phys. Chem. C* **2018**, *122*, 5040–5048.
(39) Nayak, D.; Choudhary, R. B. Augmented Optical and Electrical Properties of PMMA-ZnS Nanocomposites as Emissive Layer for OLED Applications. *Opt. Mater.* **2019**, *91*, 470–481.
(40) Aziz, S. B.; Abdullah, O. G.; Hussein, A. M.; Ahmed, H. M. From Insulating PMMA Polymer to Conjugated Double Bond Behavior: Green Chemistry as a Novel Approach to Fabricate Small Band Gap Polymers. *Polymers.* **2017**, *9*, 1–15.
(41) Aziz, S. B.; Abdullah, O. G.; Brza, M. A.; Azawy, A. K.; Tahir, D. A. Effect of Carbon Nano-Dots (CNDs) on Structural and Optical Properties of PMMA Polymer Composite. *Results Phys.* **2019**, *15*, 1–11.
(42) Sun, H.; Cao, Y.; Feng, L.; Chen, Y. Immobilizing Photogenerated Electrons from Graphitic Carbon Nitride for an Improved Visible-Light Photocatalytic Activity. *Sci. Rep.* **2016**, *6*, 1–10.
(43) Chen, W.; Yu, Y.; Zheng, X.; Qin, S.; Wang, F.; Fang, J.; Wang, G.; Wang, C.; Wang, L.; Peng, G.; Zhang, X. A. All-Carbon Based Graphene Field Effect Transistor with Graphitic Electrodes Fabricated by e-Beam Direct Writing on PMMA. *Sci. Rep.* **2015**, *5,*1–7.

TOC Graphic